POLITECNICO DI TORINO
Repository ISTITUZIONALE

# Adaptive path planning for spraying UAS in vineyard under variable wind condition

*Original*
Adaptive path planning for spraying UAS in vineyard under variable wind condition / Scagnellato, Luca; Lecce, Marco; Bloise, Nicoletta; Carreno Ruiz, Manuel; Capello, Elisa; Guglieri, Giorgio.. - (2022). (Intervento presentato al convegno ICAS 2022 - Congress of the International Council of the Aeronautical Sciences).

*Availability:*
This version is available at: 11583/2972004 since: 2022-10-03T12:26:03Z

*Publisher:*
International Council of the Aeronautical Sciences

*Published*
DOI:

*Terms of use:*

This article is made available under terms and conditions as specified in the corresponding bibliographic description in the repository

*Publisher copyright*

(Article begins on next page)

25 April 2024

33RD CONGRESS
OF THE INTERNATIONAL COUNCIL
OF THE AERONAUTICAL SCIENCES
STOCKHOLM, SWEDEN, 4–9 SEPTEMBER, 2022

ICAS 2022 SWEDEN

# ADAPTIVE PATH PLANNING FOR SPRAYING UAS IN VINEYARD UNDER VARIABLE WIND CONDITION

Luca Scagnellato[1], Marco Lecce[2], Nicoletta Bloise[1], Manuel Carreño Ruiz[1], Elisa Capello[3] & Giorgio Guglieri[3]

[1]Department of Mechanical and Aerospace Engineering, Politecnico di Torino, Italy
[2]Department of Control and Computer Engineering, Politecnico di Torino, Italy
[3]Department of Mechanical and Aerospace Engineering, Politecnico di Torino and CNR-IEIIT, Torino, Italy

## Abstract

In recent years, the evolution of technology has proven essential in the progress of agriculture mechanization towards sustainable approaches. The introduction of the Unmanned Aircraft System (UAS) is continuously growing in several agricultural operations, such as precision spraying applications of Plant Protection Products (PPP). This work aims to investigate a solution to reduce the environmental footprint during aerial spraying in an environment subject to wind field disturbance. We designed a wind estimation method to model an adaptive guidance algorithm that uses a 3D spray model realized through photos taken in an experimental testing campaign performed in a wind tunnel. The paper shows spray simulations along the rows of a vineyard obtaining satisfactory droplet deposition when the path correction algorithm is active.

**Keywords:** Unmanned Aerial Vehicle, precision spraying, navigation system, wind estimation, adaptive guidance algorithm

## 1. Introduction

In recent years, sustainable farm mechanization has become one of the key points for improving agricultural productivity and food quality. Thanks to the technological improvement, including the Internet of Things (IoT), the concept of Precision Agriculture (PA) has gained popularity, increasing the automation level in complex environments [1]. In particular, the use of Unmanned Aircraft Systems (UASs) is continuously growing for several management operations, as discussed in [2], such as mapping and monitoring to achieve also precision spraying applications of pesticides. For this last purpose, the great challenge is to identify optimal flight conditions and spray requirements to accomplish target interventions, minimizing the off-target drift problem that may cause severe environmental contamination and represents a waste of economic and natural resources. Therefore, to carry out precision spraying operations, an adaptive path planning for UAS that takes into account wind estimation should be considered, as suggested in [3].

The scenario considered in this paper is a vineyard with straight and narrow rows. Unlike the flat canopy, like rice and corn, 3D crops require more precision operations to achieve adequate pesticide droplet position and penetration. In the last decades, several studies present analyses based on lab and field testing to understand the effect of operational parameters, such as flight altitude and speed, nozzle characteristics and operating pressure, and wind speed, on spray droplet deposition, as reported in [4, 5, 6, 7, 8, 9, 10, 11]. In this regard, in [12], preliminary results are proposed in a controlled environment, the Sustainable Energy Applied Sciences, Technology, and Advanced Research (SEASTAR) Wind Tunnel at the Environment Park in Turin, Italy. During this experimental campaign, the drone was placed and fixed with its nose (x-axis) rotated clockwise by 30° with respect to the wind velocity, exactly how the UAS would fly over the vineyard row to optimize the spray coverage. After processing the images obtained in the test campaign, we are able to mathematically

describe the spray shape for different flight conditions such as wind speed and throttle setting. We define a simplified spray model by mapping shape data to the operational parameters. This model can predict droplet deposition based on wind speed, rotor velocity, and distance from the ground.
As we mentioned previously, the key and critical feature of the analyzed problem is to include the wind speed estimation in the model to evaluate the spray drift and predict the spray footprint on the ground. In agricultural fields, wind measurements are performed, employing fixed meteorological stations equipped with anemometers. In slowly changing wind conditions, performing an estimate of the local wind speed and direction at each point of the field, could be accurate enough to correct the UAS trajectory. On the other hand, if obstacles or atmospheric turbulence are present, a local wind velocity estimation is not sufficient. In UAS applications, airspeed, is typically measured through flow sensors, such as Pitot tubes or ultrasonic anemometers. The use of these devices is a cost-effective solution for local wind estimation, but they increase the multi-rotor weight and complexity and are affected by the rotors wake, as shown in [13, 14]. Furthermore, flow sensors cannot measure magnitude and direction simultaneously, and ultrasonic anemometers are sensible to rain [15].
This study presents a data-driven wind model only using data from the onboard sensors. Starting from the dynamical model of the multi-rotor and considering its control strategy, the UAS positions are correlated to the wind effects, allowing the extraction of wind magnitude and direction. This method was tested in-field, as discussed in [15] and in simulation showing satisfactory reliability, even though the vertical wind component is not studied. The tilt angle approach proposed can provide wind measurements only in hovering conditions. However, we resolve the problem using a correction based on the accelerometer measurements, as suggested in [16].
The guidance algorithm relies on the previous path planning phase. First, small UASs perform plant-to-plant disease diagnosis through multi-spectral image acquisitions of the leaves and then, Artificial Intelligence (AI) is used to accomplish the diagnostic task. Therefore, the disease recognition phase produces a prescription map containing needed plant positions in the local reference frame and their relative Plant Protection Product (PPP) demands. A Genetic Algorithm (GA) provides the UAS with the sequence of waypoints that maximize autonomy by solving a modified Salesman Problem, based on the work in [17]. This work shows a simple linear path planning above the rows of the vineyards to demonstrate the validity of the algorithm.
Then, the spraying UAS comes into play and starts flying over the vineyard, making corrections on the calculated path. The required adjustments are different depending on the target plants. The vehicle's trajectory is modified perpendicularly to the rows, using the model predictions to compensate for the sideways drift. On the other hand, the longitudinal drift is corrected by retarding or advancing in time the nozzle opening. Mixing in-field orographic and geometric analyses with a model of the PPP volume distribution, we obtain an estimation of the product deposited on the plant crown. The adaptive path planning accomplishes a more precise plant targeting, reducing the PPP environmental hazard and waste.
Finally, this work presents an innovative design of an adaptive path planning solution for UAS spraying operations in vineyards considering a dynamic wind environment. The main novelty of this work is the inclusion of the spray swath as the target position instead of using a waypoint strategy. Moreover, wind effects are included online and updating the path planning as a function of the droplet deposition. This study analyzes the droplet deposition thanks to an experimental campaign with different operational parameters.
The paper layout is the following. Section 2 shows the UASS design, its dynamics, and the guidance and control system. Section 3 contains the adaptive path planning algorithm for windy environments, describing a wind estimator strategy to implement a case as realistic as possible. Section 4 discusses simulations of the UASS adaptive path planning in a vineyard and demonstrates an improvement of droplet distribution with the path correction. Finally, we lay out our conclusions and future activities in Section 5.

## 2. Unmanned Aerial Spraying System

Following the previous work done in [18], this study defines the basic UAS architecture. The proposed vehicle is a quadcopter, chosen for its simplicity and reliability. By analyzing the current agricultural UAS available, our UAS has a 25 $kg$ as Maximum Take-Off Weight (MTOW), of which 10 $kg$ are

asigned to the spray system. From these characteristics, we defined the main geometric and inertial dimensions in Table 1. The conceptual design phase defined the motors and propellers as well: these are P30X15 propellers combined with a P80 motor ([19]) and FLAME 80A 12S ([20]) controller by T-Motor. As the battery must provide sufficient capacity and power, Li-Po batteries are chosen for this project, selecting a battery of 22000 $mAh$ of capacity made of 12 cells in series, providing a maximum voltage of 44.4 $V$.

Table 1 – Geometric and inertial characteristics

| | Value |
|---|---|
| Total mass | $25kg$ |
| Pitch moment of inertia | $0.82075kgm^2$ |
| Roll moment of inertia | $0.82075kgm^2$ |
| Yaw moment of inertia | $1.2895kgm^2$ |
| Rotor boom arm's length | $0.75m$ |

## 2.1 UASS dynamics

The quadrotor dynamics employ the classical formulation for six-degrees-of-freedom (6-DoF) systems, with kinematics and dynamics equations, as in Equations 2 and 3. These equations are expressed in two different reference frames: the body-fixed frame and the North-East-Down (NED) frame, which is considered inertial by neglecting the effects of the Earth's rotation which are orders of magnitude less than the forces developed by the vehicle [21]. First, forces and torques are calculated in the body-fixed frame, using a model based on the datasheet provided by the motor and propeller supplier [19], and then calculate the angular and linear accelerations. Then, these are integrated in time to obtain the velocities, which are then translated to the inertial frame through rotation matrices based on Euler angles, as in Equation 1. After a second integration, the UAS position and attitude are calculated and given as an input to the control system.
The rotation matrix from the body-fixed frame to the inertial reference can be written as

$$R = \begin{pmatrix} c(\theta)c(\psi) & s(\psi)s(\theta)c(\psi) - c(\phi)s(\psi) & c(\psi)s(\theta)c(\psi) + s(\phi)s(\psi) \\ c(\theta)s(\psi) & s(\phi)s(\theta)s(\psi) + c(\phi)c(\psi) & c(\phi)s(\theta)s(\psi) - s(\phi)c(\psi) \\ s(\theta) & -s(\phi)c(\theta) & -c(\phi)c(\theta) \end{pmatrix} \tag{1}$$

Whereas the gravity vector in the body-fixed frame is

$$f_g = \begin{pmatrix} -gsin(\theta) \\ gcos(\theta)sin(\phi) \\ gcos(\theta)cos(\phi) \end{pmatrix}$$

So, the complete system of equations then becomes

$$\begin{pmatrix} \dot{X} \\ \dot{Y} \\ \dot{h} \end{pmatrix} = R \begin{pmatrix} u \\ v \\ w \end{pmatrix}$$

$$\begin{pmatrix} \dot{\phi} \\ \dot{\theta} \\ \dot{\psi} \end{pmatrix} = \begin{pmatrix} 1 & s(\phi)t(\theta) & c(\phi)t(\theta) \\ 0 & c(\phi) & -s(\phi) \\ 0 & \frac{s(\phi)}{c(\theta)} & \frac{c(\phi)}{c(\theta)} \end{pmatrix} \begin{pmatrix} p \\ q \\ r \end{pmatrix}$$

$$\begin{pmatrix} \dot{u} \\ \dot{v} \\ \dot{w} \end{pmatrix} = \begin{pmatrix} rv - qw \\ pw - ru \\ qu - pv \end{pmatrix} + f_g + \frac{1}{m} \begin{pmatrix} -sign(w_x)D_X \\ -sign(w_y)D_y \\ -F - sign(w_z)D_z \end{pmatrix} \tag{2}$$

$$\begin{pmatrix} \dot{p} \\ \dot{q} \\ \dot{r} \end{pmatrix} = \begin{pmatrix} \frac{J_y - J_z}{J_x} qr \\ \frac{J_z - J_x}{J_y} pr \\ \frac{J_x - J_y}{J_z} pq \end{pmatrix} + \begin{pmatrix} \frac{1}{J_x}\tau_\phi \\ \frac{1}{J_y}\tau_\theta \\ \frac{1}{J_z}\tau_\psi \end{pmatrix} \tag{3}$$

## 2.2 Guidance and control system

The control system was modelled following a consolidated architecture based on PID controllers, as they provide sufficient performance while being very reliable and easy to tune [22]. The system consists of six different controllers, one for each degree of freedom, and are completed independent from each other as no uncoupling matrices are used. Before the mission, a *path plan* is calculated, based on the vineyard's row position and orientation, and it provides a series of waypoints that are the input for the control system. This map can be modified during the mission based on the wind conditions, as will be explained in 3.The control system architecture can be visualized in Figure 1. As

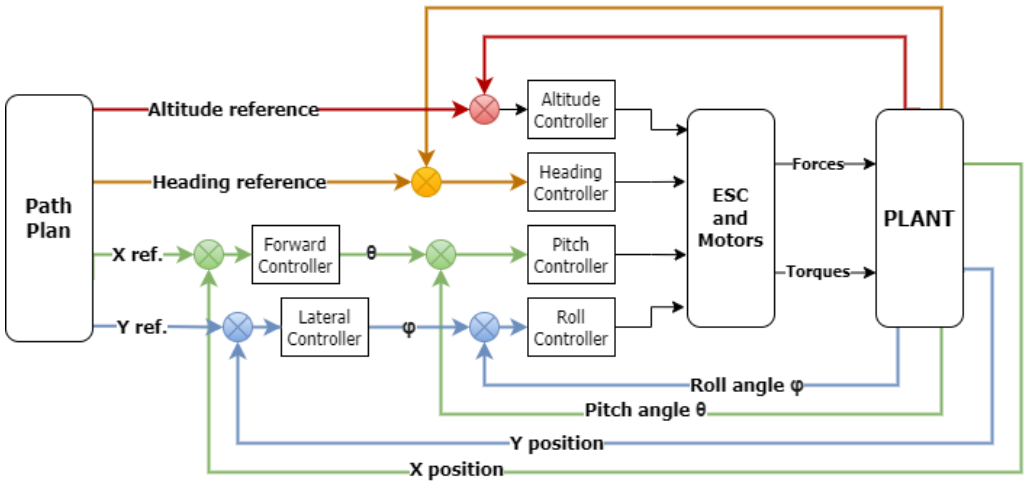


Figure 1 – Control system schematics

can be seen, the position control loop is composed of two nested loops: the outer one compares the *path plan* to the actual position and provides the inner *attitude loop* the angle references to achieve such position.

# 3. Adaptive path planning

In order to minimize the PPP dispersion so to reduce the environmental footprint of the system, it is essential to adapt the UAS operation to the environment in which it operates. As the atmospheric wind is the main factor that affects the targeting precision, it is essential to take it into account in planning and executing the spraying operation, exploiting it to deposit the protection products only where needed. This section explains the efforts to characterize the droplets trajectory and their distribution on the ground during operations and the integration of the resulting model in the guidance system.

## 3.1 Spray model and droplet distribution

A 3D-spray model of the flow distribution with the use of a hollow-cone nozzle was studied. The main objectives are to evaluate the PPP volume distribution, predict the particles deposition footprint center position and validate the model and the algorithms performed.

First, a model that predicts the deposition center position (with respect to the nozzle) is needed, in order to include it in the correction algorithm that will be discussed later. To do this, a test campaign was conducted in a wind tunnel, where multiple photos of the droplets stream were taken under different wind and rotor speed conditions, as is further described in [23]. These photos were then analyzed to obtain the second degree polynomial coefficients of the particles trajectory, as shown in Figure 2 Two regressions were then made on the coefficients of the polynomials in order to obtain a simple constant coefficients model that, given the relative wind speed and direction, the rotor *RPM* and the distance from the ground, is able to predict the spray particles deposition area with respect to the current UAS's position. The resulting Equation 4 contains $x$ the horizontal distance from the vehicle, $y$ the height from the ground and $v$ the relative wind speed.

$$x = ((aRPM + b)v + (cRPM + d))y^2 + ((eRPM + f)v + (gRPM + h))y \tag{4}$$

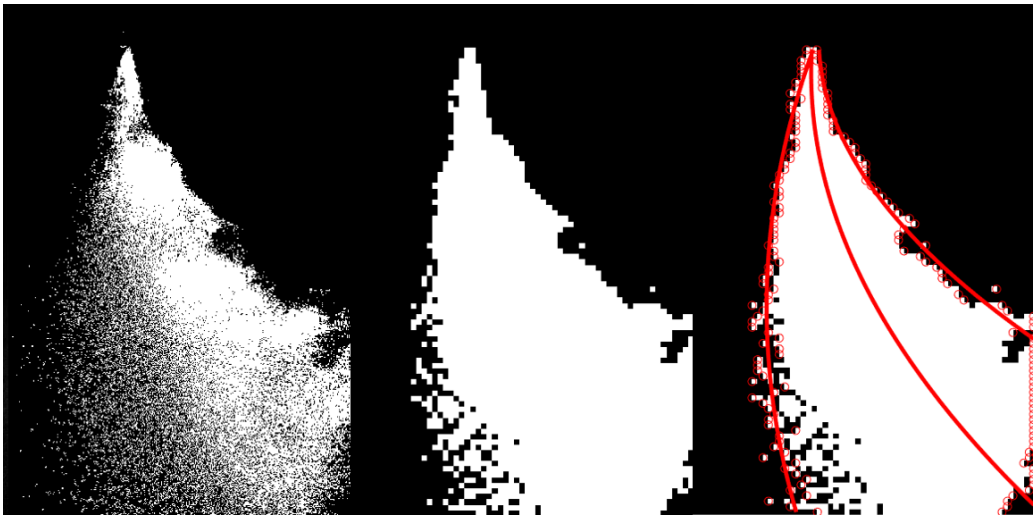

Figure 2 – Image analysis workflow ($v = 3m/s$, maximum throttle)

After having determined the deposition of the center position, the particles distribution around it must be determined. In order to do this, some assumptions are needed. Let us assume for simplicity's sake that the spray model was designed to fit a scenario in which air velocity due to the wind effect, the nozzle-ground relative velocity, and the rotor speed are null, the pressure and the flow rate have reached a stable value, and then the atomization process and the downward averaged droplets trajectories are stable. In this condition, it is reasonable to consider the hollow-cone as a conic wall with a constant and center-symmetric geometry. The spray cone produced by the nozzle has a lateral wall thickness in the order of centimeters in the proximity of the nozzle outlet, and it is supposed to gradually increase the thickness circular crown containing all the droplets moving away from the nozzle, as reported in [24] for ASJ S.r.l. nozzles. In addition, air viscosity and gravity are neglected so the direction of a generic droplet remains the same, once exits the nozzle. Following these assumptions, for a given distance from the nozzle, the droplets (and so the flow rate) could be imagined as deposited in great quantities along the circumference with radius equal to the mean of the maximum and minimum radius of the crown, and with lower quantities out of the crown. In particular, the Probability Density Function (PDF) for the droplet distribution analysis is also presented in the datasheet of the hollow-cone nozzle specification. It was modeled as a Gaussian radial basis function with a variance quadratically increasing with the distance from the nozzle and a mean equal to the mean radius of the crown (see Figure 3), i.e.

$$\sigma^2 = (\sigma_0 + \sigma_v z)^2$$

$$\begin{cases} \sigma_0 = 0,001\ m \\ \sigma_v = 0,1\ m \end{cases}$$

$$\mu = z\tan(\alpha)$$

where $\sigma_0$ and $\sigma_v$ was chosen to have a wall thickness of about $3cm$ close to the nozzle and $50cm$ at $5m$, and $\alpha$ is the spray angle of the nozzle, which depends on nozzle pressure and rotors' velocities and is inferred in real time from experimental curves.
Instead, the Gaussian radial basis function was formulated as in Equation 5 and the expression normalized by $2\pi$ is in Equation 6.

$$N\left(\mu, \sigma^2\right) = \frac{1}{\sqrt{2\pi}\sigma}\ e^{-\frac{1}{2}\frac{(r-\mu)^2}{\sigma^2}} / 2\pi \tag{5}$$

$$\int_{-\infty}^{+\infty}\int_0^{2\pi} N\left(\mu, \sigma^2\right)\ dr d\theta = 1 \tag{6}$$

From the code point of view, the model is inserted in the simulation environment to compute the actual amount of PPP released by the quadrotor when overflies the affected areas. A custom function

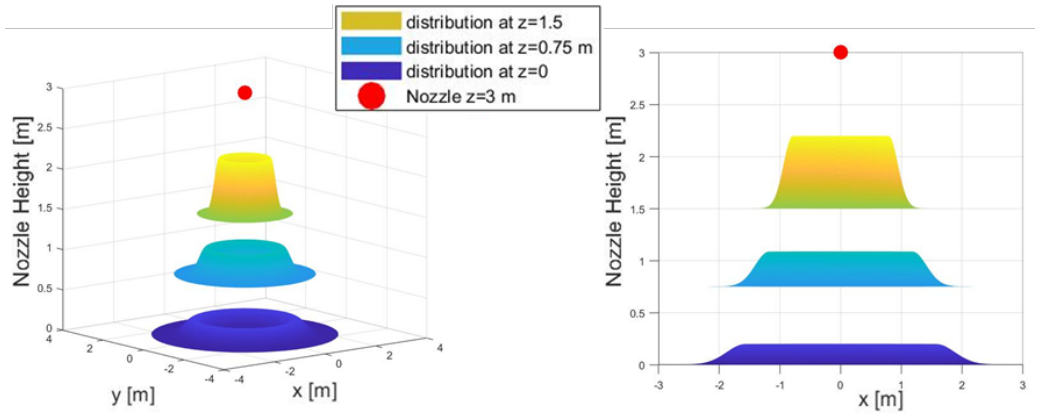


Figure 3 – Flow rate distribution in function of nozzle distance, $\omega_{rotors} = 2000rpm$, $p = 2bar$ (PDF values are qualitatively represented)

accepts as input the footprint center position at the *k-th* time step $(x,y)_{swat,\,k}$, in general different by the UAS current position, and uses it as the center of the footprint circular crown. Also knowing real time nozzle height, left equal to the drone height, $z_k$ computes the Gaussian expected value $\mu_k$ and the variance $\sigma^2{}_k$. Passing from polar to Cartesian coordinates, the bi-dimensional PDF is discretely integrated into the plane grid and multiplied by the instantaneous flow rate and the simulation sampling time, to obtain finally the released liters for each grid element. The process is repeated for the whole simulation time resulting in a complete map of the PPP sprayed in the vineyard, as reported in Figure 4.

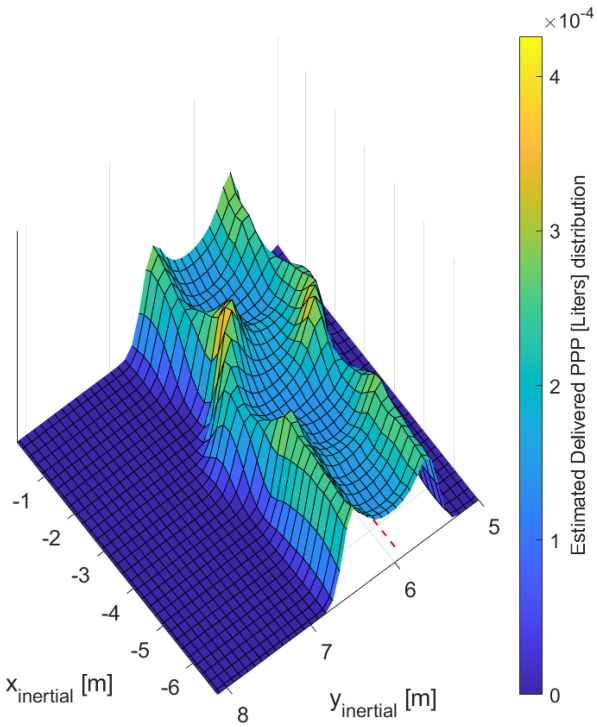


Figure 4 – PPP volume distribution in a typical row-following mission (grid thick of $8,3\ cm$)

## 3.2 Wind estimation

During the mission, a wind estimator algorithm has to be designed to evaluate the footprint center in real-time. This module, interacting with the flux profile experimental curves described above, is a key component to establish how to compensate the spray drift. Many efforts have been focused on localized wind estimation using UAS and some of them consist of onboard sensors that directly

measure air speed, although indirect measurement strategies are present in literature, as presented in [15].
The wind estimation algorithm used, called the *tilt angle approach* is based only on data provided by the onboard electronics of the UAS. Trusting the dynamical model of the quadrotor and the control strategy, it is possible to deduce a relation between the quadrotor state and the airspeed, from which wind magnitude and direction can be extracted. This method, compared to the other, does not need external sensors.
In particular, the tilt angle approach can provide wind measurements only in the hovering condition. However, the problem could be circumvented through a correction phase based on the accelerometer measurements. Using no external sensors completely surpasses the accurate and laborious positioning phase needed by direct airflow sensors, whereas mass and structure complexity are kept the same. As mentioned in [15], many studies have tried the experimentation of the tilt angle approach, obtaining results and accuracy in the order of magnitude of our interest.
Therefore, the following wind estimation algorithm is based on this work at which a correction phase is added to improve the results, as suggested in [16]. Neglecting the vertical wind component and rotors mounting tolerances, the only two reasons for which the quadrotor is tilted are i) quadrotor acceleration in *x,y* plane and ii) air-UAS velocity induced drag force compensation.
The main limitation of the following algorithm are that while the quadrotor acceleration and the tilt angle are linked by a deterministic mechanical relationship, UAS air speed drag force compensation produces a constant tilt angle at a steady state, but its transient adjustment depends on angles control and positioning estimator responsiveness. However, the assumption of instantaneous drag force compensation produced enough good results to be accepted, although some regression techniques could be used to describe a posteriori the transient phase. The above limitation is evident when the quadrotor estimates the wind in motion operations, as will be shown later. The horizontal thrust component is the vectorial sum of the horizontal drag force compensation $\overline{F_D}$ and x-y acceleration $\overline{F_{acc}}$. Figure 5 shows vectors taken into consideration for the wind estimation.

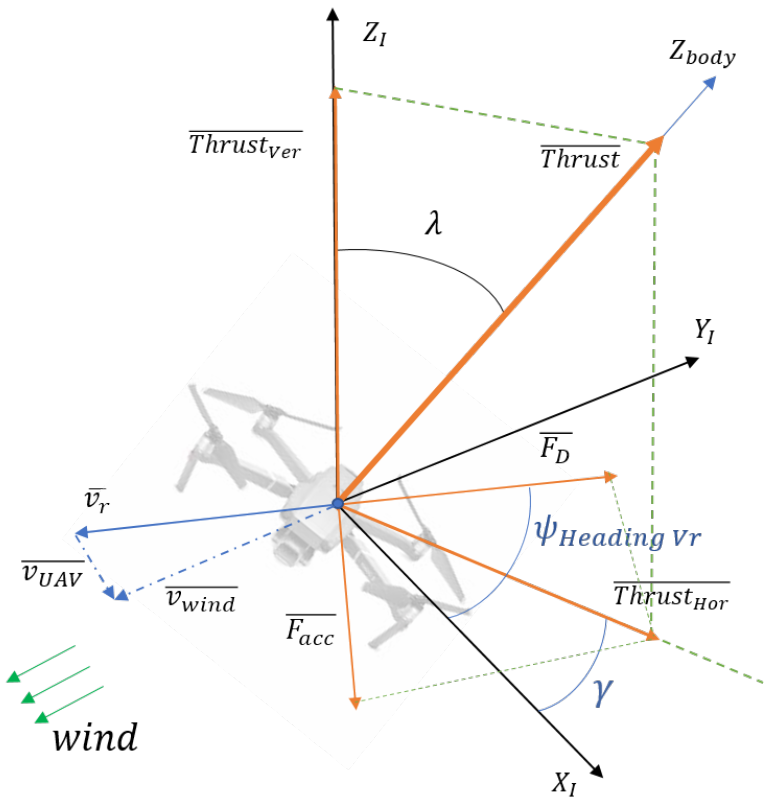


Figure 5 – Vector relationships of the wind estimation

If the vertical air resistance is neglected, the vertical thrust component magnitude, when the takeoff

is done, is equal to 7 and the horizontal is equal to 8.

$$\left|\overline{Thrust_{Ver}}\right| = m(g+\ddot{z}_I)) \tag{7}$$

$$\left|\overline{Thrust_{Hor}}\right| = m(g+\ddot{z}_I)\tan(\lambda) \tag{8}$$

The tilt angle $\lambda$ is estimated inverting the relation of the scalar product between $z_I$ and $z_{body}$

$$|\lambda| = |\mathrm{acos}(\cos(\phi)\ \cos(\theta)\ )|$$

where $\phi$ is the roll angle, $\theta$ the pitch angle and $\varphi$ the yaw angle of the ZYX Euler triad.
Whereas the heading angle $\gamma$ of $\overline{Thrust_{Hor}}$ is computed as the arctangent of the ${z_{body}}^I$ components on the inertial horizontal plane

$$\gamma = atan2\left(\frac{\mathrm{c}(\phi)\ \mathrm{s}(\theta)\ s(\psi)-\mathrm{s}(\phi)\ \mathrm{c}(\psi)}{\mathrm{c}(\phi)\ \mathrm{c}(\theta)\ c(\psi)+\mathrm{s}(\phi)\ \mathrm{s}(\psi)}\right)$$

At this point, angles and $\overline{Thrust_{Hor}}$ are known and the $\overline{F_D}$ vector can be derived from the relationship

$$\overline{F_D} = -\overline{F_{acc}} + \overline{Thrust_{Hor}}$$

where $\overline{F_{acc}}$ can be directly measured by rotating the accelerometer measurements in the inertial reference frame, neglecting the vertical acceleration and multiplying the resulted vector by the UAS mass. At the best the control system can do, the $\overline{F_D}$ force (9) is equal and opposite to the drag force exerted by the horizontal air velocity relative to the UAS.

$$\left|\overline{F_D}\right| = \tfrac{1}{2}\rho C_D(\lambda) A_{proj}(\lambda)\left|\overline{v_r}\right|^2 \tag{9}$$

where

$$\begin{cases} \rho = 1{,}225\ Kg/m^3 & air\ density\ in\ standard\ condition \\ C_D(\lambda) & Air\ flow\ drag\ coefficient \\ A_{proj}(\lambda) & UAS\ exposed\ surface\ projection \\ \overline{v_r} & (x,y)\ air-UAS\ relative\ velocity \end{cases}$$

So $\overline{v_r}$ is estimated in magnitude and direction

$$\begin{cases} \left|\overline{v_r}\right| = \sqrt{\frac{2\left|\overline{F_D}\right|}{\rho C_D(\lambda) A_{proj}(\lambda)}} \\ \angle\overline{v_r} = \psi_{Heading\ Vr} + \pi \end{cases}$$

The 2D wind velocity vector (in the horizontal plane) is finally estimated knowing the horizontal UAS inertial velocity outputted by the Kalman filter

$$\overrightarrow{v_{wind}} = \overrightarrow{v_{UAS}} + \overrightarrow{v_r}$$

Therefore, $\overline{F_D}$ can be computed the portion of the tilt angle engaged to contrast the air drag force, i.e. the angle between the projection of the ${z_{body}}^I$ axis on the vertical plane containing $\overline{F_D}$ and the $z_I$ axis and it simply results in Equation 10.

$$\lambda_{F_D} = atan(\left|\overline{F_D}\right|, \left|\overline{Thrust_{Ver}}\right|) \tag{10}$$

We need to compute $C_D(\lambda)$ in a reliable way CFD analysis fused with wind tunnel tests. The drag coefficient is derived measuring the drag force exerted by a controlled air speed for different tilt angles and different rotors velocities (to considering the effects of blades induced turbulence). Instead to compute $A_{proj}(\lambda)$, a 3D design of the UAS body could be used to project the exposed area in the vertical plane toward which the quadrotor is facing. However, to give a first estimate of those two crucial parameters a simplified geometry of the UAS is used to model them. Modeling the quadrotor as a cylinder of radius $l/2$ and height $h$ the tilt angle is used to orient the 3D shape in the space. Where $l = 0{,}65\ m$ and $h = 0{,}3\ m$ in our case. For small 2D accelerations the corrected tilt angle $\lambda_{F_D}$ can be confused with the tilt angle $\lambda$, so the tilting direction of the cylinder is the same direction of

$\overline{F_D}$. The projected surface $A_{proj}$ is limited between its maximum, namely the base circular surface of the cylinder, and the minimum given by the rectangular surface projected by the semi-lateral surface of the cylinder.

$$\begin{cases} A_{proj}(90^\circ) = \pi\left(\frac{l}{2}\right)^2 = A_{proj,\max} \\ A_{proj}(0^\circ) = hl = A_{proj,\min} \end{cases}$$

Between this interval, the circle is projected as an ellipse with semi-major axes equal to $l$ and semi-minor axes equal to $l\,\sin(\lambda)$ , whereas the lateral semi-surface is approximated as a rotated rectangle projection.

$$A_{proj}(\lambda) = hl\,|\cos(\lambda_{F_D})\,| + |\sin(\lambda_{F_D})\,|\,\pi\left(\frac{l}{2}\right)^2$$

For the drag coefficient function, we used the theoretical drag coefficient for Reynolds numbers in the range ($10^4 - 10^6$) of three extreme cases and then we interpolated as in Equation 11.

1. for $\lambda_{F_D} = 0^\circ$ the lateral surface of a cylinder is exposed at the laminar flux, the $C_D(0^\circ) = 1,17$
2. for $\lambda_{F_D} = 90^\circ$ the flat base surface is exposed so $C_D(90^\circ) = 1,17$
3. for $\lambda_{F_D} = 45^\circ$ the prism assumes a configuration assimilated to a cuboid tilted of 45°, with $C_D(45^\circ) = 0,8$.

$$C_D(\lambda_{F_D}) = 0,985 + 0,185\cos(4\,\lambda_{F_D}) \tag{11}$$

Table 2 – Wind estimation errors

| | **Wind magnitude estimation Root Mean Squared Error (RMSE) [m/s]** | **Wind direction estimation RMSE [°]** |
|---|---|---|
| **Static/Constant wind** | 0,21 | 4,5 |
| **Static/Variable wind** | 0,23 | 12,7 |
| **Dynamic/Variable wind** | 0,51 | 8,61 |

Finally, to validate the algorithm, a simulation was performed with an ideal simulated constant-magnitude/constant-direction wind of $4m/s$ coming from the north, so with a wind vector angle of $-270°$. Whereas, the second simulation was done with a wind mean of $4m/s$, a wind standard deviation of $2m/s$, a gust with zero mean and standard deviation equal $0.3m/s$, a direction with mean $-270°$ and a variance of $40°$. In both cases, the UAS estimates the wind in hovering, a static condition. Therefore, a third simulation was performed, in which the drone follows a classic serpentine path (dynamic situation) and, meanwhile, estimates the wind magnitude and direction, as reported in Table 2. In Figure 10, an example of wind estimation results in magnitude and direction (heading angle in the horizontal plane) compared to the simulated wind is reported. Can be noticed that until the UAS takes off (about first 10 seconds) the estimation is not reliable because of numerical fluctuations in accelerations and attitude computed by the model and the Extended Kalman Filter, so those estimation samples were not included in the error computation.

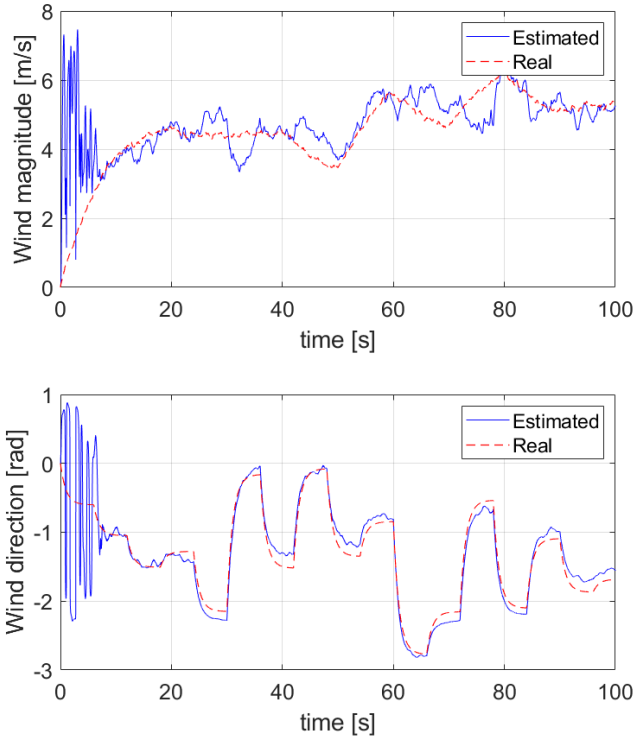


Figure 6 – Wind magnitude and direction estimation for the dynamic case with variable wind

### 3.3 Path correction under wind effects

Once a reliable wind estimation is available, together with the spray model previously discussed, is was possible to develop a correction algorithm that takes into account these data to minimize the particles drift, optimizing the deposition on the plants. As shown in Figure 7, the correction is achieved in two different ways

- the first one directly acts on the vehicle position, by modifying the *path plan* and moving the UAS laterally with respect to the length of vine rows
- the second one controls the particles deposition indirectly by turning on and off the spray circuit when needed. Based on the spray model, the system is capable to predict where the particles will deposit: if the deposition area overlaps the target zone, the nozzle opens, otherwise it shuts off.

This strategy is needed because, if the correction were to be achieved only by controlling the position, any sudden wind change in the longitudinal direction (concerning the row's length) would make the vehicle swing back and forth and hence over-spraying the underlying plants, reducing the overall accuracy.

## 4. Simulation and results

The path correction algorithm can be seen in action in Figures 8 and 9. In Figure 8, the lateral correction is made evident, and the quad-rotor position is shifted in the opposite direction with respect to the wind, and by a distance proportional to the wind intensity, illustrated in Figure 10. In Figure 9, the second correction can be seen, as the timing of turning on and off of the spray circuit is shifted with respect to the planned values.

This correction is also responsible for shutting down the spray circuit when the vehicle is moving from one row to the next one. It is also able to temporarily shut the circuit off when the wind suddenly changes in the lateral direction and the vehicle isn't able to adjust its position right away, as can be observed in the second bottom row of Figure on the right 11. Finally, comparing Figures 11, it is evident how this logic improves the system accuracy, as the product is consistently deposited on the

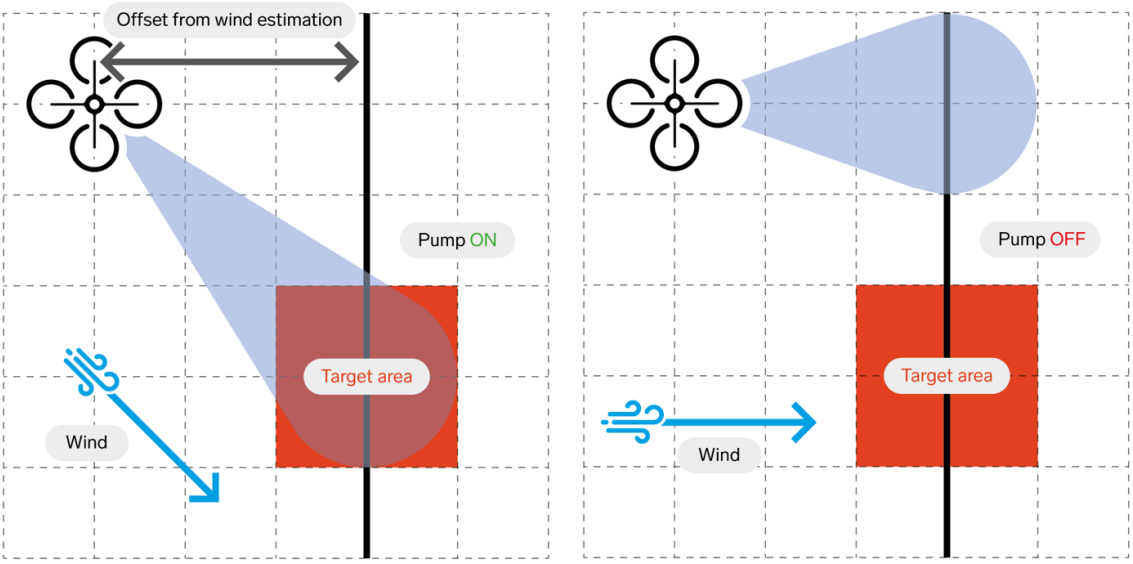


Figure 7 – Path correction

plants while, when the path correction algorithm is not active, the deposition precision is severely degraded and it seldom targets the vine rows.

## 5. Conclusion

In conclusion, this work presents a solution for UAS aerial spray application to maximise the deposition on the plants, minimising the drift problem between the rows of the vineyard. The results of this research move in the direction of greater precision and automation perfectly in line with the principles of Agriculture 4.0. In fact, once the UAS trajectory has been defined off-line, thanks to an adaptive guidance algorithm it is possible to guarantee a real time correction through onboard sensor and the wind estimation with a good accuracy.

Here, through detailed simulations, the combination of the tilt angle approach with the Kalman filter allows us to demonstrate that it is a good strategy to meet this challenge. In particular, the relative path correction able to adapt to the wind estimation guarantees an important improvement on the PPP droplet distribution on the plants which otherwise reaching undesired areas.

Future works will be focused on verifying the time required to estimate the wind disturbances by sensors and then recalculate the UAS trajectories considering the spray model. Finally, an experimental test campaign will be interesting to validate this work.

## 6. Contact Author Email Address

nicoletta.bloise@polito.it

## 7. Copyright Statement

The authors confirm that they, and/or their company or organization, hold copyright on all of the original material included in this paper. The authors also confirm that they have obtained permission, from the copyright holder of any third party material included in this paper, to publish it as part of their paper. The authors confirm that they give permission, or have obtained permission from the copyright holder of this paper, for the publication and distribution of this paper as part of the ICAS proceedings or as individual off-prints from the proceedings.

## References

[1] A. Khanna and S. Kaur, “Evolution of internet of things (iot) and its significant impact in the field of precision agriculture,” *Computers and electronics in agriculture*, vol. 157, pp. 218–231, 2019.

[2] P. Radoglou-Grammatikis, P. Sarigiannidis, T. Lagkas, and I. Moscholios, “A compilation of UAV applications for precision agriculture,” *Computer Networks*, vol. 172, p. 107148, 2020.

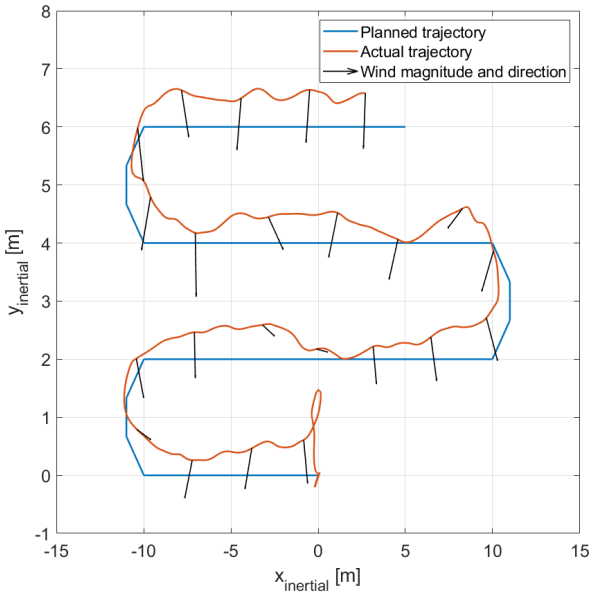


Figure 8 – Vehicle trajectory compared to the vine rows' position

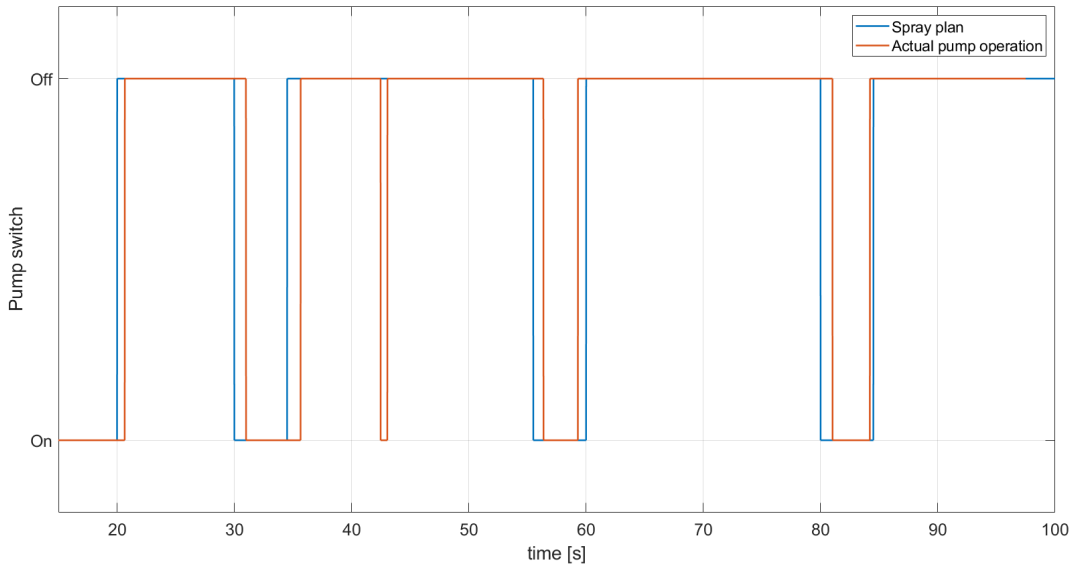


Figure 9 – Spray timing correction

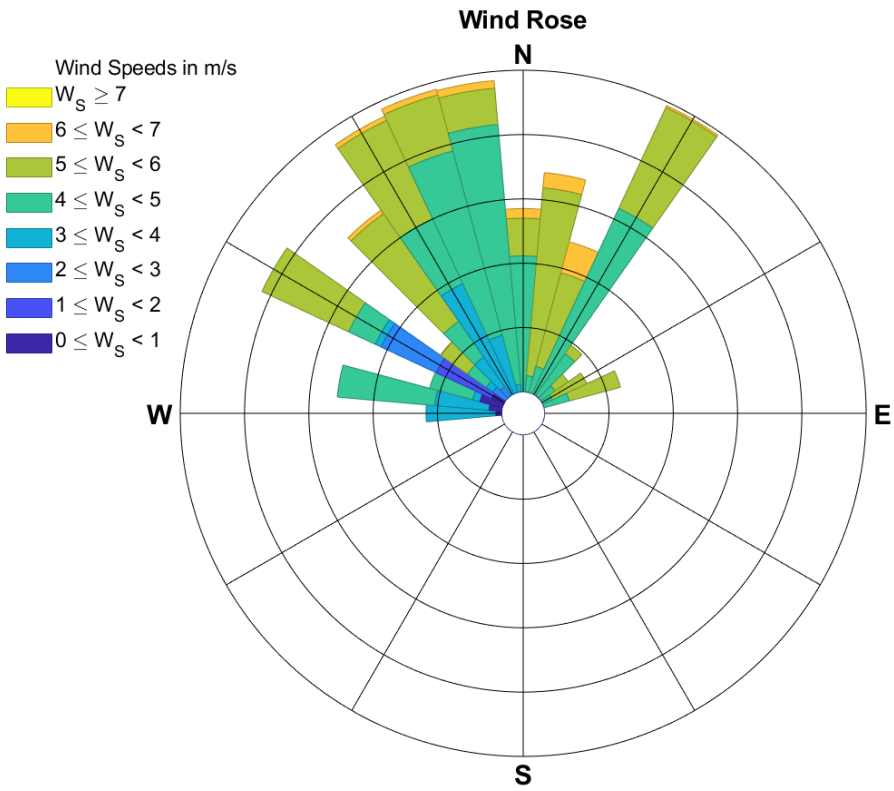


Figure 10 – Wind rose of the simulations

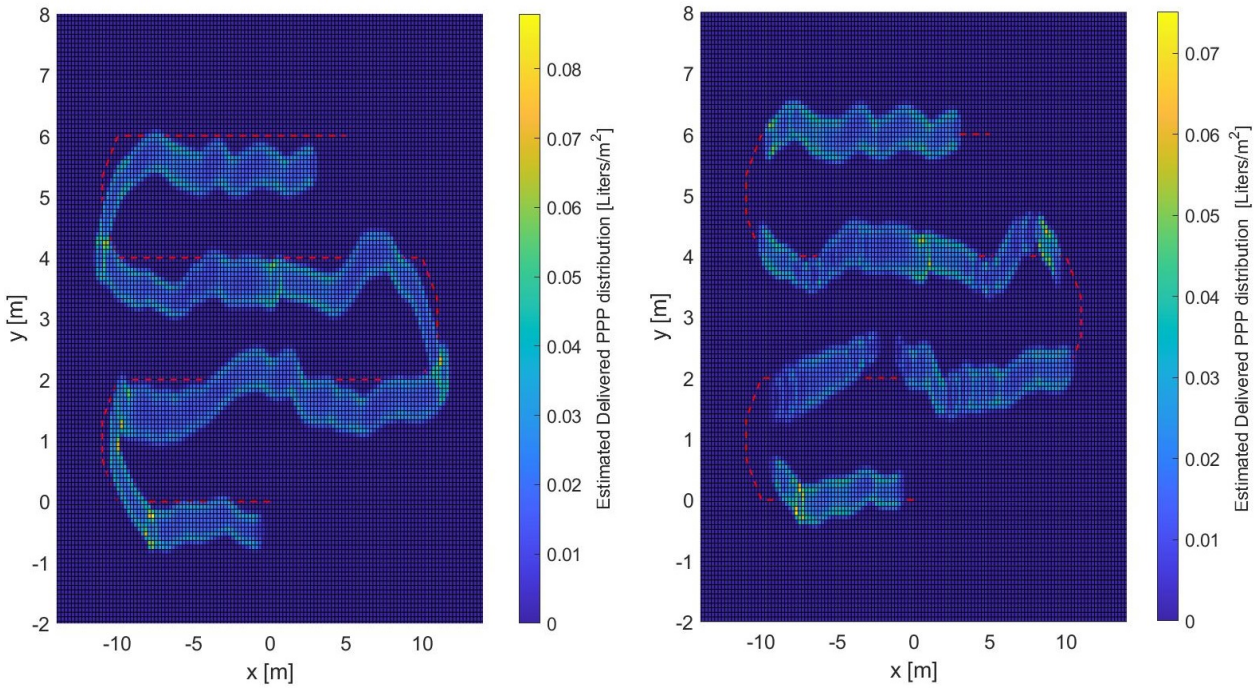


Figure 11 – PPP plant distribution without and with spray adaptive control system

[3] B. S. Faiçal, H. Freitas, P. H. Gomes, L. Y. Mano, G. Pessin, A. C. de Carvalho, B. Krishnamachari, and J. Ueyama, "An adaptive approach for uav-based pesticide spraying in dynamic environments," *Computers and Electronics in Agriculture*, vol. 138, pp. 210–223, 2017.

[4] D. Nuyttens, K. Baetens, M. De Schampheleire, and B. Sonck, "Effect of nozzle type, size and pressure on spray droplet characteristics," *Biosystems engineering*, vol. 97, no. 3, pp. 333–345, 2007.

[5] S. Guo, J. Li, W. Yao, Y. Zhan, Y. Li, and Y. Shi, "Distribution characteristics on droplet deposition of wind field vortex formed by multi-rotor uav," *PloS one*, vol. 14, no. 7, p. e0220024, 2019.

[6] M. N. A. Kharim, A. Wayayok, A. R. M. Shariff, A. F. Abdullah, and E. M. Husin, "Droplet deposition density of organic liquid fertilizer at low altitude uav aerial spraying in rice cultivation," *Computers and Electronics in Agriculture*, vol. 167, p. 105045, 2019.

[7] D. Sarri, L. Martelloni, M. Rimediotti, R. Lisci, S. Lombardo, and M. Vieri, "Testing a multi-rotor unmanned aerial vehicle for spray application in high slope terraced vineyard," *Journal of Agricultural Engineering*, vol. 50, no. 1, pp. 38–47, 2019.

[8] S. Chen, Y. Lan, Z. Zhou, F. Ouyang, G. Wang, X. Huang, X. Deng, and S. Cheng, "Effect of droplet size parameters on droplet deposition and drift of aerial spraying by using plant protection uav," *Agronomy*, vol. 10, no. 2, p. 195, 2020.

[9] F. Ahmad, B. Qiu, X. Dong, J. Ma, X. Huang, S. Ahmed, and F. A. Chandio, "Effect of operational parameters of uav sprayer on spray deposition pattern in target and off-target zones during outer field weed control application," *Computers and Electronics in Agriculture*, vol. 172, p. 105350, 2020.

[10] G. Wang, Y. Han, X. Li, J. Andaloro, P. Chen, W. C. Hoffmann, X. Han, S. Chen, and Y. Lan, "Field evaluation of spray drift and environmental impact using an agricultural unmanned aerial vehicle (uav) sprayer," *Science of the Total Environment*, vol. 737, p. 139793, 2020.

[11] J. Martinez-Guanter, P. Agüera, J. Agüera, and M. Pérez-Ruiz, "Spray and economics assessment of a uav-based ultra-low-volume application in olive and citrus orchards," *Precision Agriculture*, vol. 21, no. 1, pp. 226–243, 2020.

[12] N. Bloise, M. C. Ruiz, D. D'Ambrosio, and G. Guglieri, "Wind tunnel testing of remotely piloted aircraft systems for precision crop-spraying applications," in *2021 IEEE International Workshop on Metrology for Agriculture and Forestry (MetroAgriFor)*. IEEE, 2021, pp. 378–383.

[13] T. A. Johansen, A. Cristofaro, K. Sørensen, J. M. Hansen, and T. I. Fossen, "On estimation of wind velocity, angle-of-attack and sideslip angle of small uavs using standard sensors," in *2015 International Conference on Unmanned Aircraft Systems (ICUAS)*. IEEE, 2015, pp. 510–519.

[14] W. Thielicke, W. Hübert, U. Müller, M. Eggert, and P. Wilhelm, "Towards accurate and practical drone-based wind measurements with an ultrasonic anemometer," *Atmospheric Measurement Techniques*, vol. 14, no. 2, pp. 1303–1318, 2021.

[15] P. Abichandani, D. Lobo, G. Ford, D. Bucci, and M. Kam, "Wind measurement and simulation techniques in multi-rotor small unmanned aerial vehicles," *IEEE Access*, vol. 8, pp. 54 910–54 927, 2020.

[16] Y. Song, Q.-H. Meng, B. Luo, M. Zeng, S.-G. Ma, and P.-F. Qi, "A wind estimation method for quadrotors using inertial measurement units," in *2016 IEEE International Conference on Robotics and Biomimetics (ROBIO)*. IEEE, 2016.

[17] L. Becce, N. Bloise, and G. Guglieri, "Optimal path planning for autonomous spraying uas framework in precision agriculture," in *2021 International Conference on Unmanned Aircraft Systems (ICUAS)*. IEEE, 2021, pp. 698–707.

[18] N. Bloise, M. C. Ruiz, D. D'Ambrosio, and G. Guglieri, "Preliminary design of a remotely piloted aircraft system for crop-spraying on vineyards," *2020 IEEE International Workshop on Metrology for Agriculture and Forestry (MetroAgriFor). IEEE*, pp. 1–6, 2020.

[19] [Online]. Available: https://store.tmotor.com/goods.php?id=783

[20] [Online]. Available: https://store.tmotor.com/goods.php?id=830

[21] C. Jekeli, *Inertial Navigation Systems with Geodetic Applications*. De Gruyter, 2001.

[22] M. Malik and N. Sehgal, "A comparative study of classical and modern controllers," *International Journal of Engineering Research and Technology (IJERT)*, vol. 5, 2017.

[23] N. Bloise, M. C. Ruiz, D. D'Ambrosio, and G. Guglieri, "Wind tunnel testing of remotely piloted aircraft systems for precision crop-spraying applications," *2021 IEEE International Workshop on Metrology for Agriculture and Forestry (MetroAgriFor). IEEE*, 2021.

[24] D.M.Tamagnone, P.Balsari, and D. G. Oggero, "Servizio di accertamento delle caratteristiche funzionali e della sicurezza delle macchine agricole," 2016.